Chemical Science

ROYAL SOCIETY OF CHEMISTRY

EDGE ARTICLE

View Article Online
View Journal | View Issue

Cite this: *Chem. Sci.*, 2023, **14**, 1852

All publication charges for this article have been paid for by the Royal Society of Chemistry

Received 7th December 2022
Accepted 19th January 2023

DOI: 10.1039/d2sc06732c

rsc.li/chemical-science

Photo-controllable heterostructured crystals of metal–organic frameworks *via* reversible photocycloaddition†

Xin-Da Huang,‡[a] Ben-Kun Hong,‡[b] Ge-Hua Wen,[a] Shu-Hua Li*[b] and Li-Min Zheng*[a]

Metal–organic framework (MOF)-based heterostructures are attractive because they can provide versatile platforms for various applications but are limited by complex liquid epitaxial growth methods. Here, we employ photolithography to fabricate and control MOF-based heterostructured crystals *via* [4 + 4] photocycloaddition. A layered dysprosium–dianthracene framework, $[Dy(NO_3)_3(depma_2)_{1.5}]\cdot(depma_2)_{0.5}$ (**2**) [$depma_2$ = pre-photodimerized 9-diethylphosphonomethylanthracene (depma)] underwent a single-crystal-to-single-crystal transition at 140 °C to form $[Dy(NO_3)_3(depma)(depma_2)]\cdot(depma_2)_{0.5}$ (**3**). The dissociated anthracene moieties are face-to-face π–π interacted allowing a reversible photocycloaddition between **2** and **3**. This structural transformation causes a luminescence switch between blue and yellow-green and thus can be used to fabricate erasable **2** + **3** heterostructured crystals for rewritable photonic barcodes. The internal strain at the heterostructure interface leads to photobending and straightening of the crystal, a photomechanical response that is fast, reversible and durable, even operating at 140 °C, making it promising for photoactuation. This work may inspire the development of intelligent MOF-based heterostructures for photonic applications.

Introduction

Heterostructures have attracted considerable attention in recent years because they can create novel and multifunctional platforms to achieve desired functions and applications. Metal–organic frameworks (MOFs) are a promising class of materials that have tunable structures and can be designed to introduce specific physicochemical properties.[1] MOF-based heterostructured crystals are typically prepared by a bottom-up epitaxial growth method, which is the crystallization of one structure on the surface of another structure.[2] This method has some limitations, such as the need to select highly lattice-matched MOFs, the difficulty in controlling heterostructure patterns, the inability to erase and reuse them, and the complicated preparation process. To overcome these limitations, an effective approach is to prepare MOF-based heterostructured crystals precisely by external stimulation, but to our knowledge, related studies have scarcely been reported.[3]

We envision that MOFs incorporating photosensitive and photochromic components are excellent choices for this purpose, as light offers unique advantages such as easy access, and rapid and precise operability.[4,5] To this end, anthracene and its derivatives are appealing ligands because they can experience reversible [4 + 4] photocycloaddition reactions upon UV light irradiation, accompanied by significant photochromic behaviour.[6] However, a prerequisite for such a reversible photocycloaddition reaction to occur is a face-to-face π–π stacking of anthracene units with a spacing of less than 4.2 Å, which is hard to satisfy in the anthracene-based MOF system because the self-assembly of the MOF is usually dominated by coordination bonds rather than π–π interactions.[7] An alternative approach is to use pre-synthesized dianthracene ligands as linkers to construct the metal–dianthracene frameworks.[8] After UV light irradiation or thermal annealing, the dianthracene ligands dissociate to form a pair of anthracene units, which can be further used for the photocycloaddition reaction. Unfortunately, previous studies have demonstrated that de-dimerization of dianthracene ligand often leads to the slip of the two anthracene groups and the destruction of single crystallinity,[8a–e] making it difficult to attain a reversible photocycloaddition reaction for the fabrication of erasable heterostructures.

We envisage that reversible photocycloaddition reactions can be achieved in the dianthracene-based MOFs when the framework

[a]*State Key Laboratory of Coordination Chemistry, School of Chemistry and Chemical Engineering, Collaborative Innovation Centre of Advanced Microstructures, Nanjing University, Nanjing 210023, China. E-mail: lmzheng@nju.edu.cn*

[b]*Institute of Theoretical and Computational Chemistry, School of Chemistry and Chemical Engineering, Nanjing University, Nanjing 210023, China. E-mail: shuhua@nju.edu.cn*

† Electronic supplementary information (ESI) available: Experimental details, crystallographic details, and full characterization (SC-XRD, PXRD, IR, UV-vis and photoluminescence spectra, thermal analysis, photographs) of all described compounds. CCDC 2214247–2214250. For ESI and crystallographic data in CIF or other electronic format see DOI: https://doi.org/10.1039/d2sc06732c

‡ These authors contributed equally to this work.

reaches a delicate balance of rigidity and flexibility. Herein, we report a dysprosium–dianthracene framework, $[Dy(NO_3)_3(depma_2)_{1.5}]\cdot(depma_2)_{0.5}\cdot CH_3OH$ (**1**), where $depma_2$ is pre-photodimerized 9-diethylphosphonomethylanthracene (depma). Compound **1** has a two-dimensional (2D) honeycomb-like layer structure in which the Dy^{III} ions are connected by flexible $depma_2$ linkers. These layers are stacked to form a framework containing hexagonal channels where the lattice $depma_2$ and methanol molecules reside. The encapsulated guest $depma_2$ molecule enhances the backbone rigidity of **1**. Interestingly, **1** underwent two consecutive thermally induced single-crystal-to-single-crystal (SC–SC) phase transitions, first forming $[Dy(NO_3)_3(depma_2)_{1.5}]\cdot(depma_2)_{0.5}$ (**2**) below 80 °C and then $[Dy(NO_3)_3(depma)(depma_2)]\cdot(depma_2)_{0.5}$ (**3**) at 140 °C. Further increase in temperature led to complete dissociation of the dianthracene ligands and collapse of the framework structure, forming the mononuclear compound $Dy(NO)_3(depma)_3$ (**4**) at 160 °C.[9] Impressively, the partially dissociated phase **3** has a one-dimensional (1D) zigzag chain structure, where the dissociated anthracene moieties are face-to-face π–π interacted. As a result, a reversible photocycloaddition reaction was realized between **2** and **3** in an SC–SC manner, accompanied by a photoluminescence (PL) change between blue and yellow-green. Based on this reversible photocycloaddition reaction, we developed a strategy *via* the photolithography technique for the precise and controllable fabrication of MOF-based heterostructures, which is further used for photonic applications such as photonic barcoding and photomechanical response. To our knowledge, this is the first example of MOF-based heterostructures that can be used for rewritable photonic barcoding. It is also the first example of MOFs showing photomechanical response that can repeatedly operate above 100 °C.

Results and discussion

Crystal structure of 1

The stoichiometric reaction of $Dy(NO_3)_3\cdot 6H_2O$ and $depma_2$ in CH_3OH/CH_2Cl_2 at room temperature resulted in compound **1**. Single crystal X-ray structure analysis revealed that compound **1** crystallized in the triclinic space group $P\bar{1}$ (Table S1†). The asymmetric unit consists of one Dy^{III}, three NO_3^-, four half $depma_2$ and one methanol molecule (Fig. S1a†). Each Dy^{III} is coordinated to nine oxygen atoms, three from the three independent $depma_2$ and six from three chelated nitrate anions. The Dy–O bond lengths fall in the range 2.295(4)–2.487(3) Å, and the O–Dy–O bond angles lie between 51.6(2)and 153.2(1) ° (Table 1 and S2†). There are four crystallographically distinct $depma_2$; each one is located at an inversion center. Three of them ($depma_2$-A, -B, -C) serve as two-connected linkers to bridge metal centers into a honeycomb-like layer in the *ac* plane (Fig. 1a). The fourth ($depma_2$-D) is encapsulated as a guest molecule in the channel generated by the layer stacking. The Dy–Dy distances over the $depma_2$ ligands are 14.88, 15.21 and 14.24 Å for $depma_2$-A, -B, and -C, respectively. The central C–C bond lengths are 1.638(6) Å (C2–C9A) for $depma_2$-A, 1.634(5) Å (C21–C28B) for $depma_2$-B, 1.640(6) Å (C40–C47C) for $depma_2$-C, and 1.638(7) Å (C59–C66D) for $depma_2$-D (Table 1). The layer has a (3,2)-connecting topology and can be viewed as composed of edge-sharing hexamer rings of $[Dy_6(depma_2)_6]$ (Fig. 1a and S1b†). The size of the hexamer ring is *ca.* 11.4 Å × 15.4 Å, which is sufficient to accommodate the guest molecules of one $depma_2$ and two methanols. These guest molecules are stabilized in the lattice by C–H···O and O–H···O hydrogen bonds and C–H···π interactions with the coordinated $depma_2$-C ligands (Fig. 1a and S1c†).

SC–SC structural transformation

Thermal gravimetric (TG) analysis showed that the as-prepared compound **1** lost one molecule of methanol below 100 °C (obs. 1.97%, calcd. 1.89%), followed by a plateau between 100 and 200 °C (Fig. S2a†). The differential scanning calorimetry (DSC) curve showed an endothermic peak near 80 °C, and two exothermic peaks near 130 °C and 166 °C (Fig. S2b†). The endothermic peak is due to the removal of methanol molecules (enthalpy $\Delta H = 51.7$ kJ mol^{-1}). In contrast, the two exothermic peaks are attributed to the de-dimerization of $depma_2$ ligands

Table 1 Selected structural parameters for compounds **1–4**

	1	**2**	**3**	**4**[a]
Space group	$P\bar{1}$	$P\bar{1}$	$P\bar{1}$	$P\bar{1}$
a (Å)	12.058(1)	12.017(2)	12.132(1)	11.547(1)
b (Å)	13.858(1)	13.485(2)	13.334(1)	13.173(1)
c (Å)	23.233(1)	23.445(3)	23.308(2)	21.025(1)
V (Å^3)	3835.5(2)	3762.6(10)	3745.4(5)	2891.2(2)
Dy–O (Å)	2.295(4)–2.487(3)	2.288(5)–2.481(5)	2.290(4)–2.487(4)	2.314(2)–2.510(2)
O–Dy–O (°)	51.6(2)–153.2(1)	51.7(2)–153.5(2)	51.0(2)–153.1(1)	51.5(1)–153.9(1)
C2–C9A (Å) ($depma_2$-A)	1.638(6)	1.634(7)	1.632(6)	3.730
C21–C28B (Å) ($depma_2$-B)	1.634(5)	1.627(8)	1.631(6)	5.782
C40–C47C (Å) ($depma_2$-C)	1.640(6)	1.622(9)	3.60	5.049
C59–C66D (Å) ($depma_2$-D)	1.638(7)	1.657(14)	1.632(6)	—
Intralayer Dy–Dy (Å)[b]	14.88, 15.21, 14.24	14.71, 15.21, 14.11	14.63, 15.24, 13.83	15.97, 19.41, 13.69
Shortest interlayer Dy–Dy (Å)	12.06	12.02	12.13	9.356
Interlayer distance (Å)	8.40	8.34	8.37	8.35

[a] Ref. [9]. [b] The Dy–Dy distance over the dianthracene bridge.

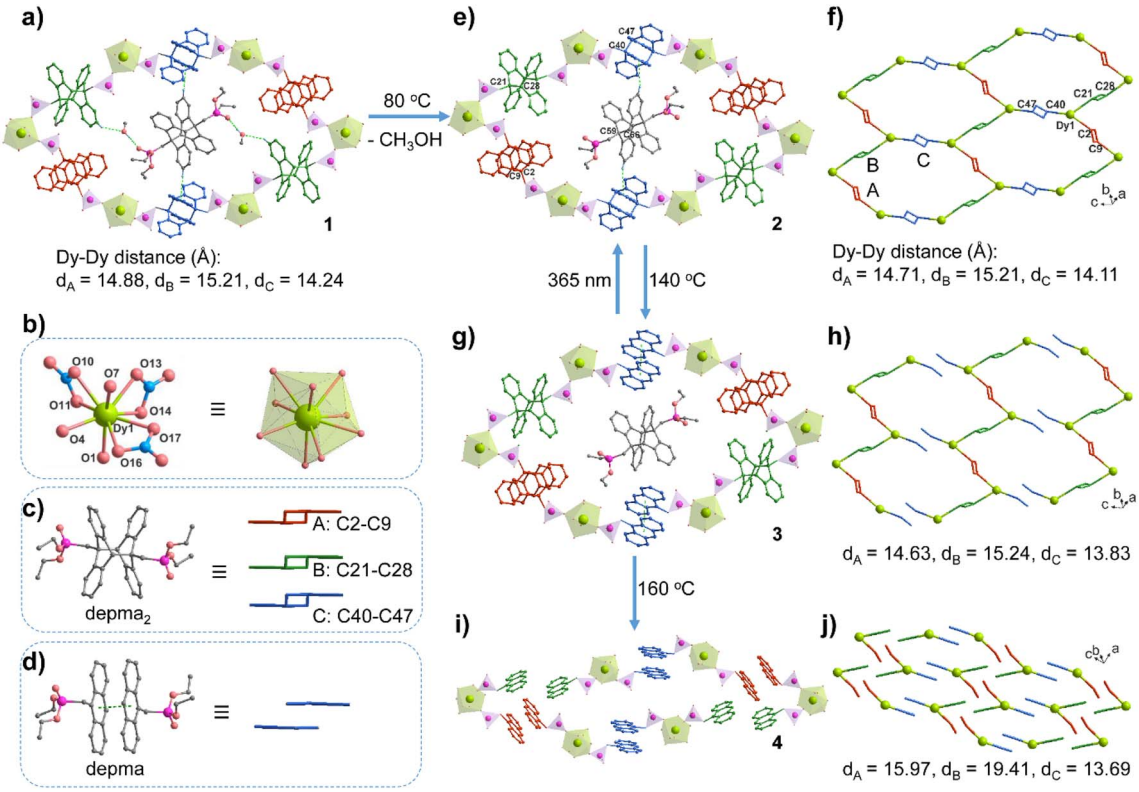

Fig. 1 The structural transformation from **1** to **2** to **3** to **4**. (a) The $[Dy_6(depma_2)_6]$ hexamer ring with encapsulated $depma_2$ and methanol guests in the layered structure of **1**. The green dotted lines represent the hydrogen bonds between the guest and framework $depma_2$ ligands. (b) The coordination environment of the Dy1 atom in structure **1**. (c) The three types of $depma_2$ linkers in the framework of **1** with the simplified forms in different colors (red for $depma_2$-A, green for $depma_2$-B, and blue for $depma_2$-C). (d) The dissociated $depma_2$-C ligand in structure **2** and its simplified form. (e and f) The hexamer ring and layer topology in structure **2**. (g and h) The hexamer ring and supramolecular layer topology in structure **3**, where zigzag chains contain alternating $depma_2$-A and -B linkers, which are further stacked by $\pi-\pi$ interactions between depma ligands dissociated from $depma_2$-C. (i and j) The mononuclear structure of **4** stacking in the lattice. Adapted from ref. 9.

(enthalpy $\Delta H = -25.0$ and -72.1 kJ mol^{-1}). The dissociation of the $depma_2$ ligand is supported by the infrared (IR) spectra of the samples treated at 140 °C and 160 °C (Fig. S3†), which show a peak at 1247 cm^{-1} characteristic of the C–H in-plane bending vibration of dissociated anthracene units.[6] Apparently, the thermally triggered de-dimerization of $depma_2$ proceeds in two steps rather than simultaneously. Noting that there are four independent $depma_2$ in the structure, the question arises as to which $depma_2$ in the structure dissociates first.

To examine the structural changes during the thermal treatment, we kept the crystals of **1** in air at room temperature for two days (or heating at 80 °C for 5 min) to obtain the desolvation phase $[Dy(NO_3)_3(depma_2)_{1.5}]\cdot(depma_2)_{0.5}$ (**2**). When the temperature was increased to 140 °C and 160 °C, respectively, and held for 5 min, we obtained the new phases $[Dy(NO_3)_3(depma)(depma_2)]\cdot(depma_2)_{0.5}$ (**3**) and $Dy(NO)_3(depma)_3$ (**4**) (major phase, Fig. S4†), respectively. Impressively, the structural transformation from **1** to **2** to **3** was carried out in an SC–SC manner, which allowed the structural analyses of **2** and **3** by the single-crystal diffraction method.

Like **1**, compound **2** adopts the triclinic space group $P\bar{1}$ (Table S1†). It shows a similar layer structure to **1** except for the absence of lattice methanol molecules. The release of the methanol guest leads to cell volume contraction [3762.6(10) Å^3 *vs.* 3835.9(2) Å^3 for **1**]. However, the differences in bond lengths and angles of the dysprosium ion are small. For **2**, the Dy–O bond lengths and O–Dy–O angles are 2.288(5)–2.481(5) Å [*vs.* 2.295(4)–2.487(3) Å for **1**] and 51.7(2)–153.5(1)° [*vs.* 51.6(2)–153.2(1)° for **1**], respectively (Table 1 and S2). The Dy–Dy distances over the $depma_2$ (-A, -B, -C) bridges are 14.71, 15.21, and 14.11 Å, among which that over the $depma_2$-C is the shortest. The C–H$\cdots\pi$ interactions are still present between the guest $depma_2$-D molecules and coordinated $depma_2$-C ligands (Fig. 1e and S5†). Notably, the DSC curve of **2** showed two exothermic peaks attributed to the de-dimerization of $depma_2$ ligands (enthalpy $\Delta H = -24.4$ and -73.8 kJ mol^{-1}) (Fig. S2b†), which is consistent with that of **1**.

Remarkable structural change was observed for compound **3**. This compound remains in the same space group $P\bar{1}$. In contrast to **1** and **2**, one kind of dianthracene linkers ($depma_2$-C) de-dimerizes in **3**, forming face-to-face stacked anthracene moieties (Fig. 1g and S6†). The dissociation of $depma_2$-C also leads to a slight contraction of the unit cell in **3** [3745.4(5) Å^3 *vs.* 3762.6(10) Å^3 for **2**], and a small change of the Dy–O bond lengths [2.290(4)–2.487(4) Å] and O–Dy–O angles [51.0(2)–153.1(1) °] (Table 1 and S3†). But the central C40–C47C distance

of depma$_2$-C is strikingly elongated from 1.640(6) to 3.60 Å. The Dy–Dy distance over depma$_2$-C is also shortened from 14.11 Å in **2** to 13.83 Å in **3**. No C–H$\cdots\pi$ interactions between the guest depma$_2$-D and the de-dimerized depma$_2$-C can be found. Clearly, upon heating to 140 °C the layer structure of **2** was dissociated into a zigzag chain structure of **3** in which the Dy atoms are alternatively bridged by depma$_2$-A and depma$_2$-B ligands (Fig. 1h). The reason why it is depma$_2$-C and not the other three kinds of ligands that first undergoes thermally induced de-dimerization is rationalized by theoretical calculations as shown below. Noting that the dissociated anthracene groups in **3** are face-to-face interacted with a separation of 3.60 Å, it is possible to reverse the process *via* a photocycloaddition reaction to form **2**. Indeed, irradiation of crystals of **3** with 365 nm LED UV light (*ca.* 100 mW cm^{-2}) at room temperature for 0.5 h gave rise to the colorless crystals of **2**, confirmed by the single crystal structural analysis (Tables S1 and S5†). We conjecture that the realization of the reversible SC–SC photocycloaddition reaction between **2** and **3** may be related to the presence of the guest depma$_2$-D, which pillars the adjacent depma$_2$-C ligands within the [Dy$_6$(depma$_2$)$_6$] hexamer ring and interacts with the depma$_2$-C ligands *via* weak C–H$\cdots\pi$ contacts, whereby a delicate balance of rigidity and flexibility may have been achieved. To our knowledge, the reversible SC–SC photocycloaddition reaction in anthracene-based coordination polymers has not been documented in the literature.[10]

Compound **4** was obtained as a yellow powder, the structure of which was previously reported.[9] It has a mononuclear structure wherein each dysprosium ion is linked by three NO_3^- and three depma (Fig. 1i and j). As for its three asymmetric anthracene units, only one of them maintains face-to-face π–π interactions with the anthracene ring in the adjacent monomer, thus ruling out the possibility of a reverse structural transformation from **4** to **3**.

Finally, one might ask whether UV light shorter than 300 nm can trigger the structural transformation from **2** to **3**. We prepared **2UV** by exposing compound **2** to 280 nm LED UV light (*ca.* 100 mW cm^{-2}) for 5 min. The UV-vis spectrum of **2UV** is similar to that of **3** (Fig. S7†). The IR spectrum of **2UV** shows weak vibrational bands at 1247 and 903 cm^{-1}, ascribed to the in-plane and out-of-plane bending vibrations of the C–H bonds of the anthracene unit (Fig. S8†). However, the PXRD pattern of **2UV** is identical to the original **2** (Fig. S9†), indicating that the light-induced dissociation of dianthracene in **2** is far from complete and may occur only on the surface. Extending the light exposure time to 1 h did not bring significant changes.

Theoretical calculations

The selective dissociation of depma$_2$-C in compound **2** after thermal treatment is crucial for our material because it makes it possible to achieve a reversible structural transformation between **2** and **3** in an SC–SC manner. In contrast, other reported coordination polymers with dianthracene units suffered from a fatal collapse of the framework upon thermally induced de-dimerization. Therefore, uncovering the cause of selective dissociation is essential for further exploration of light-responsive coordination polymers with dianthracene units. To this end, periodic DFT calculations were performed using the Vienna *Ab initio* Simulation Package (VASP) code[11] with the projector augmented wave (PAW) method[12] at the gamma point. The PBE method[13] was adopted with D3 (BJ) dispersion correction.[14] The kinetic energy cutoff was chosen to be 450 eV and the Hubbard $U_f = 5.0$ eV was employed for Dy.[15] The non-spin-polarized calculations have been tested to be reasonable in this work.

Crystals **2** and **3** (dissociated depma$_2$-C) were fully optimized with their X-ray structures (obtained at 140 °C) as initial structures. Based on the optimized structure of **2**, depma$_2$-C was scanned along the double reaction coordinates C40–C47′ and C40′-C47 (distance from 1.637 Å to 3.552 Å) and the energy profile is shown in Fig. 2. This process is highly exothermic by 37.3 kJ mol^{-1}, with a reasonable electronic energy barrier of 50.6 kJ mol^{-1}. Similarly, the optimized structures of the dissociated depma$_2$-A, -B and -D, as well as the energy profile of the dissociation of depma$_2$-A, were estimated and the results are listed in Tables S6–S8.† For the dissociation of depma$_2$-A, the electronic energy barrier is estimated to be 67.6 kJ mol^{-1}, and the overall reaction is exothermic by 8.4 kJ mol^{-1}. The dissociation processes of depma$_2$-B ($\Delta E = -1.9$ kJ mol^{-1}) and depma$_2$-D ($\Delta E = 34.8$ kJ mol^{-1}) are less energetically favorable or unfavorable. Overall, the pathway with the lowest electronic energy barrier is the dissociation of depma$_2$-C, which follows the experimental result.

The selectivity is dominated by the steric hindrance. By analyzing the optimized structure of **3**, we found that the distance between the anthracene planes d(C40–C47′) is 3.552 Å, which is consistent with the distance (3.600 Å) between two anthracene planes in the experimental crystal of **3** and the calculated equilibrium distance of two anthracene molecules in the gas phase (3.551 Å) at the same theoretical level. For the dissociated depma$_2$-A, -B, and -D, the distances between the two anthracene planes in the optimized crystal structures are 3.388 Å, 3.217 Å and 3.399 Å, respectively, indicating that there exists steric hindrance between two anthracene planes. This is because the dissociations of the dianthracene planes of

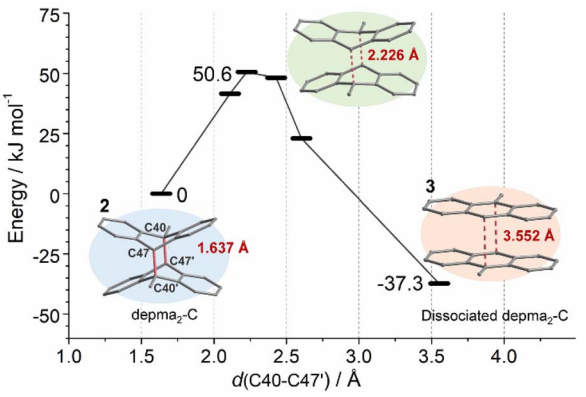

Fig. 2 DFT-computed energy profile for the dissociation of depma$_2$-C.

depma$_2$-A, -B or -D (Fig. S10–S12†) are hindered by the rigid framework while the same process in the case of depma$_2$-C is not hindered by the neighboring framework. Hence, our calculations can account for the fact that only the dissociation of depma$_2$-C was observed at 140 °C.

The dissociation temperature of depma$_2$-C is lower than that of other coordination polymers linked by dianthracene units,[8a–c] but slightly higher than that of dianthracene compounds given by the solid-state photodimerization reaction of metal–anthracene complexes.[6,7a] The latter may stem from the fact that *in situ* topochemical photocycloaddition of two coplanar anthracene units may release a looser lattice environment than depma$_2$-C. The unique structural transformation and the resulting change in luminescence properties allow the material to have a variety of applications, such as molecular switches, barcodes, and photomechanical actuators based on optically programmable heterostructures.

Switching of photoluminescence

The reversible structural transformation associated with the central C–C cleavage/formation of the dianthracene ligand would lead to a significant change in its optical properties. Compounds **1** and **2** are colorless while **3** is yellow. The fluorescence images under 365 nm UV light clearly reveal that compounds **1** and **2** emit blue light while compound **3** displays yellow-green emission (Fig. 3a). The results indicate that the emission color can be reversibly switched between **2** and **3** *via* thermal treatment at 140 °C and 365 nm light illumination.

To investigate the optical properties of **1–3** in-depth, we measured their UV-vis and PL spectra. As shown in Fig. S7,† the UV-vis diffuse reflectance spectrum for compound **1** exhibits several absorption peaks in the range of 300–420 nm because of the Frank–Condon vibration. The strong absorption band at *ca.* 286 nm is attributed to the π → *π transition of the ligand depma$_2$. The small peaks at 757 nm are assigned to the f–f transition of Dy^{III} ion from $^6H_{15/2}$ to $^6F_{3/2}$ states. Fig. 3b and S13† give the PL spectra of **1** which show five peaks at 398, 420, 442, 475 and 574 nm. The first four originate from the vibrational manifold of the π ← *π transition of dianthracene, and the lifetime of the peak at 420 nm is $\tau = 5.3$ ns. The peak at 573 nm is attributed to the f–f transition of the Dy^{III} ion from $^4F_{9/2}$ to $^6H_{13/2}$, which is verified by its long lifetime of 72.7 μs (Table S9 and Fig. S14†). Apparently, the excited dimeric ligand depma$_2$ can sensitize the dysprosium emission, but the sensitization efficiency is low, so that blue light can be observed with the naked eye.

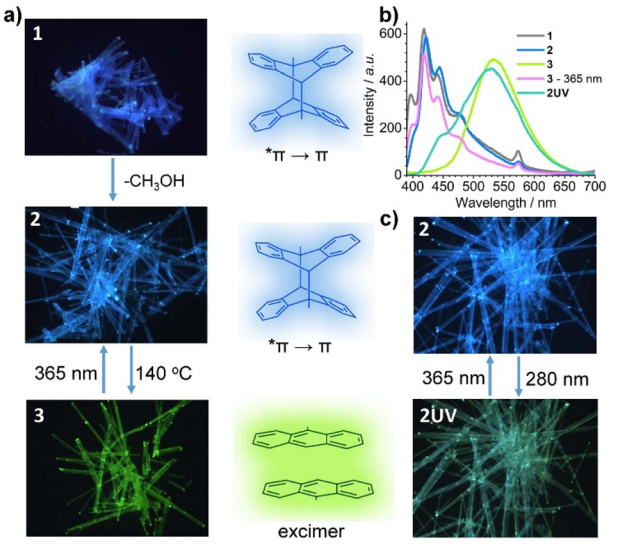

Fig. 3 (a) The photoluminescence switching from **1** to **2** to **3**. (b) The emission spectra excited at 365 nm for compounds **1**, **2**, **2UV**, **3** and its irradiated sample with 365 nm UV light. (c) The reversible photoluminescence switching from **2** to **2UV** upon UV light irradiation.

The desolvation phase **2** shows almost the same absorption and emission spectra as **1**. For compound **3**, the absorption intensity at *ca.* 286 nm decreases and a strong and broad absorption band appears between 300 and 480 nm which is red-shifted compared to those of **1** and **2**. In addition, compound **3** shows a completely different emission profile (Fig. 3b and S13c†), where a broad peak emerges at 535 nm, in line with the observed yellow-green emission. The broad peak is ascribed to the excimer emission arising from the two face-to-face π–π interacted anthracene moieties with a lifetime of 42.3 ns (Fig. S14†). Interestingly, although only one of the four dianthracene ligands was dissociated in **3**, no emission peak corresponding to dianthracene was visualized. Continuous irradiation of **3** with 365 nm UV light caused the excimer emission at 535 nm to fade out, and the vibronic peaks of dianthracene at 398, 420, 442, and 475 nm to reappear. This is consistent with the photodimerization of the anthracene units in **3** leading to the regeneration of compound **2**.

We also measured the emission spectrum of **2UV**. As shown in Fig. 3b and S15,† it has two main peaks at 446 and 526 nm and two shoulders at 485 and 574 nm. The peak at 446 nm is attributed to the π ← *π transition of the undissociated dianthracence units. The peak at 526 nm originates from the excimer emission of the face-to-face π–π interacted anthracene moieties. The two very weak shoulder peaks at 485 and 574 nm originate from the Dy^{III} center. The simultaneous observation of the three types of emission in **2UV** further demonstrates that only a small amount of the dianthracene ligands in **2** dissociates under 280 nm light. As a result of the combination of the three types of emission, compound **2UV** emits green light (Fig. 3c), unlike **3** which emits yellow-green light. Interestingly, **2UV** can be converted back to **2** after exposure to 365 nm UV light and the emission spectrum reverts to that of **2**. Thus, reversible luminescence switching between **2** and **2UV** can be achieved by alternating exposure to 280 nm and 365 nm UV light.

Photogenerated heterostructured crystals

The reversible SC–SC structural transformation between **2** and **3** and the resulting luminescence switch suggest that this MOF material may be used to construct erasable heterostructures with potential applications in photonic barcoding.

We first selected a rod-shaped crystal (**A**: 466 × 27 × 20 μm^3) of **1** and heated it to 140 °C to obtain a crystal of **3**. Then, the crystal was covered with a photomask with parallel slits and

exposed to 365 nm UV light for 2 min (Fig. 4a and S16†). The resulting crystal maintained a smooth surface and transparency. The photograph taken in the reflectance mode showed continuous segments that are alternately yellowish and colorless (Fig. 4b, inset). The faint yellow color comes from compound **3**, whereas the colorless species is the photogenerated compound **2**. The fluorescence image of the crystal clearly showed alternating yellow-green (bright) and blue (dark) domains corresponding to compounds **3** and **2**, respectively. The result indicates that the multi-segment heterostructured crystal of **3** + **2** with bright and dark stripes can be successfully fabricated by photolithography. More interestingly, single yellow-green emission can recover after thermal annealing of heterostructured crystal (Fig. S16†), meaning that the heterostructure can be generated and erased through alternative UV light irradiation and thermal annealing of the crystal of **3**.

We then investigated the possibility of producing heterostructured crystals by irradiating the photomask crystal **2** (**B:** 701 × 32 × 16 μm^3) with 280 nm light. As shown in Fig. S17 and S18,† the fluorescence image of the resulting crystal shows a clear sequence of green and blue regions, where the green color corresponds to the partially de-dimerized product **2UV**. Interestingly, this new heterostructured (**2** + **2UV**) crystal can be erased and regenerated by alternately exposing it to 365 nm and 280 nm UV light.

Noting that the known MOF-based heterostructures were normally fabricated in solution *via* the epitaxial growth method, the photolithography method developed in this work possesses several significant advantages.[16] First, the fabrication process is much faster and more convenient. The heterostructure can be generated *in situ* simply by UV light irradiation for several minutes. Second, the pattern of the heterostructure can be easily controlled by specific design of the photomask. Finally, the heterostructure is erasable *via* thermal annealing or UV light irradiation. These advantages make the material an outstanding candidate for the fabrication of rewritable barcodes with complicated stripes on-demand *via* photolithography technology.

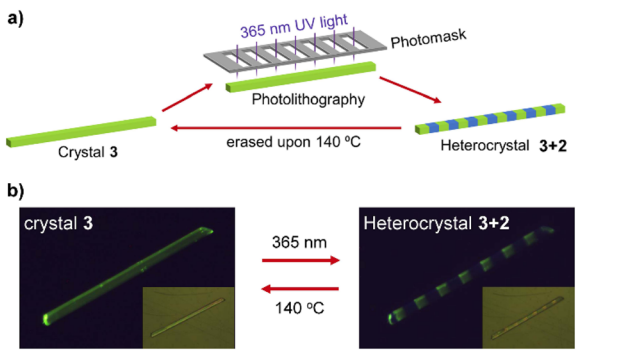

Fig. 4 (a) Scheme to show the photolithography process to fabricate and erase the heterostructured crystal **3** + **2**. (b) The fluorescence graphs showing the switching between the crystal **3** (left) and heterostructured crystal consisting of sequent **2** and **3** blocks (right). The inset displays their optical pictures.

Reversible photomechanical response

The reversible SC–SC structural transformation between **2** and **3** also allows for their application as photomechanical actuators. In order to observe the photomechanical effect more clearly, we chose elongated crystals of **3** for our study. We fixed one end of a needle-like crystal of **3** (**C:** 477 × 10 × 7 μm^3) on a glass plate and monitored its photo-induced deformation through a microscope under light (bright field) or darkness (dark field) (Fig. 5a). After irradiation with 365 nm UV light, crystal **C** bent towards the incident light, reaching a maximum displacement of 70.6 μm at its other end at 14 s, with a deflection angle of 9.8° (Fig. 5a, S19 and Video S1†). It then bent away from the incident light and recovered its straight shape, but with a significant deviation from the original position, with a slight contraction of 6.2 μm (*ca.* 1.3%) along the long axis of the crystal.

Photo-induced bending of crystals usually arises from internal strain at the interface of the reactant–product heterostructure after an incomplete photochemical reaction.[17] When the rod-like crystal was irradiated with vertical UV light, the crystal bent toward or away from incident light depending on lattice contraction or elongation of the product phase along the long axis of the crystal. The crystal face indexing shows that the long axis of our needle-like crystal extends along the direction of the *a*-axis, which is also the layer stacking direction, while the *b*-axis and *c*-axis are almost perpendicular to the long-axis direction of the crystal (Fig. S20†). According to the above-mentioned crystal structure description, the photodimerization reaction of compound **3** to form **2** is accompanied by unit cell expansion (by 0.4%) and shortening of the *a*-axis (by 0.9%) (Table 1). Thus, the incomplete photodimerization reaction of crystal **3** can produce **2** + **3** heterostructures and accumulate internal strains, which drive the bending deformation of the crystal (Fig. 5d). When the photodimerization reaction is completed to produce **2**, this internal strain is released, leading to the re-straightening of the crystal.[18] The resulting straightened crystal of **2** shrinks by 1.3% along the long axis (*a*-axis) compared to the original crystal of **3**.

Clearly, the complete transformation from **3** to **2** causes the shortening of the needle-like crystal and significant deviation from the initial position. Thermal annealing at 140 °C can restore the crystal of **3** to its initial state. Due to the reversibility of the photocycloaddition reaction, the thermally recovered crystal of **3** can be bent and straightened again under 365 nm light (Fig. 5a and Video S2†), accompanied by a change in luminescence from bright yellow-green to blue.

To further investigate the photo-driven bending effect of crystal **3** at elevated temperature, we put another needle-like crystal **D** (426 × 7 × 6 μm^3) onto a hot stage with the temperature kept at 140 °C and irradiated with a 365 nm UV light from the upper left (Fig. S21a and Video S3†). It was found that crystal **D** underwent rapid photo-induced bending and strengthening at 140 °C, with the degree of bending reaching a maximum at 3 s of exposure and returning to a straight shape at 12 s of exposure. This response is much faster than that at room temperature (Fig. S21b and Video S4†). It is of interest that although the temperature of 140 °C leads to dissociation of the dianthracence unit, the photodimerization reaction still occurs

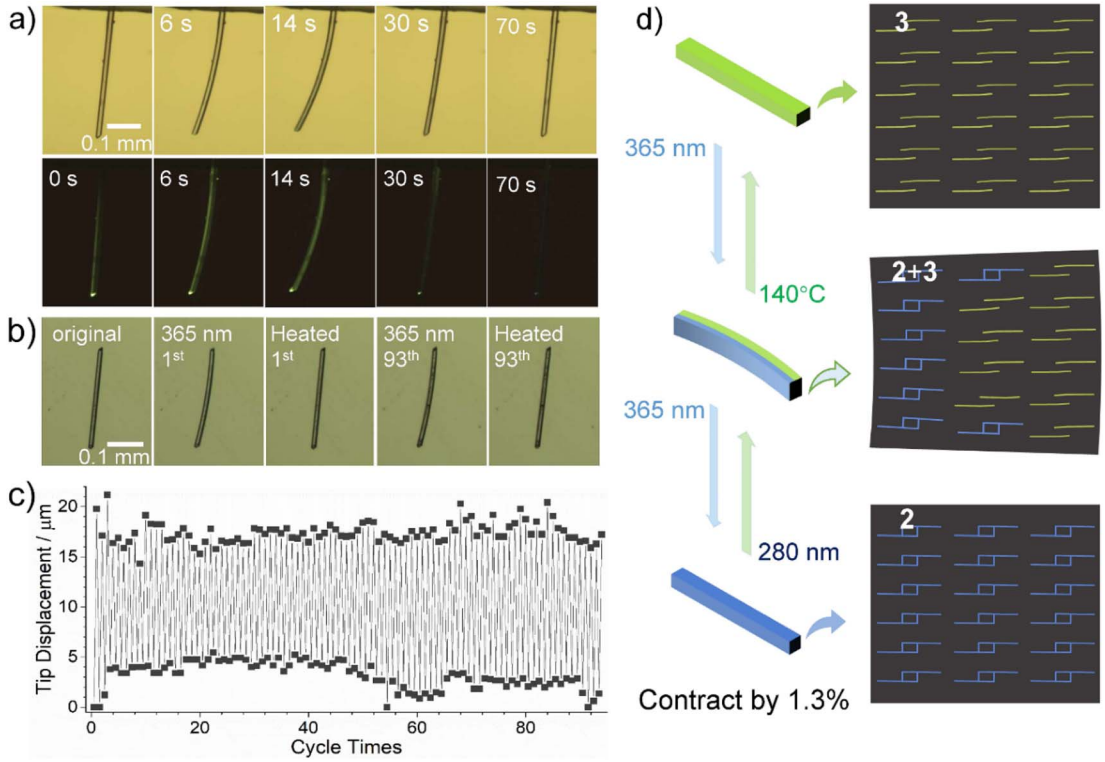

Fig. 5 (a) The observed photobending deformation of crystal **C** upon irradiation with 365 nm UV light two times, respectively taken under lamp light (top) and in the dark (down). (b) The photograph and (c) tip displacement of the repeated photobending deformation for crystal **E** ($310 \times 7 \times 6\ \mu m^3$) of compound **3** through alternate irradiation with 365 nm UV light for 4 s and thermal annealing at 140 °C for 2 min. (d) Photomechanical bending and contraction of the rod-like crystal resulted from gradual changes from pure **3** to the heterostructure of **2** and **3**, to pure **2**.

at 140 °C and its reaction rate is faster than that at room temperature. After turning off the UV light after the exposure of 3 s, the bent crystal straightened within 3 min at 140 °C (Fig. S22a and Video S5†). These results indicate that crystals of **3** can achieve a rapid and reversible photomechanical motion through alternating 365 nm light illumination and thermal annealing, both at 140 °C. The reversible photomechanical behavior can also be realized at other temperatures except for different annealing times, *i.e.*, 12 min at 120 °C, 5 min at 130 °C, and 2 min at 150 °C (Fig. S22b†).

To verify the excellent fatigue resistance of the process, we selected another crystal of **3** (**E**: $310 \times 7 \times 6\ \mu m^3$) and studied its photomechanical properties by 365 nm light illumination at 20% power for 4 s and thermal annealing at 140 °C for 2 min alternatively. The results demonstrate that this reversible process can be repeated for at least 93 cycles without significant tip displacement change (Fig. 5b and c). It is worth mentioning that coordination polymers showing reversible photomechanical motion have not been reported before,[19] though a few discrete metal–organic complexes were found to show photomechanical effects, such as bending, popping, jumping, and peeling (Table S10†).[20] Impressively, the reversible photomechanical motion can be processed at high temperatures above 100 °C; this phenomenon has never been documented for metal–organic systems.

The photomechanical properties can also be observed using alternative 280 nm and 365 nm light sources due to the slight dissociation of $depma_2$ upon exposing the crystal of **2** to 280 nm UV light. As shown in Fig. S23,† when the crystal of **2** (**F**: $368 \times 7 \times 5\ \mu m^3$) was exposed to 280 nm UV light (20% powder) from the left side, it bent away from the light source and reached a maximum within 8 s with a tip displacement of $d_2 = 42\ \mu m$, corresponding to the formation of a **2+3** heterostructure. Then, we switched the light source to 365 nm UV light, the bent crystal **F** became almost straight again within 10 s, but with a small deviation from the original one ($d_1 = 6\ \mu m$). Thus, the reversible light-induced bending and straightening can be achieved by alternating irradiation with 280 nm and 365 nm UV light (Video S5†). We repeated this process at least 16 times and found that the tip displacement change (Δd) decreased linearly after each cycle (t), obeying the equation $\Delta d = -0.851\ t + 37.8\ \mu m$ (Fig. S24†). This means that the reversibility will disappear around $t = 44$ cycles. The faster fatigue of this photobending driven only by UV light could come from unavoidable damage to the crystal. Nevertheless, our deformable crystal stands out among MOFs for its multi-stimulus response, bidirectional motion and fluorescence changes.

Conclusions

We report a new two-dimensional dysprosium-organic framework $[Dy(NO_3)_3(depma_2)_{1.5}]\cdot(depma_2)_{0.5}\cdot CH_3OH$ (**1**), where the Dy^{III} ions are linked by three types of dianthracene ligands ($depma_2$-A, -B, -C). One of them ($depma_2$-C) in the

desolvation phase $[Dy(NO_3)_3(depma_2)_{1.5}]\cdot(depma_2)_{0.5}$ (**2**) can be selectively dissociated by thermal annealing at 140 °C, which is rationalized by the DFT calculation, forming $[Dy(NO_3)_3(depma)(depma_2)]\cdot(depma_2)_{0.5}$ (**3**). Compound **3** has a one-dimensional zigzag chain structure in which the dissociated anthracene moieties are face-to-face π–π interacted. Reversible SC–SC structural transformation between **2** and **3** was visualized by alternative thermal annealing and 365 nm UV light irradiation, accompanied by the luminescence change between blue and yellow-green. In addition, incomplete structural transformation between **2** and **3** was achieved using light irradiation only with alternative 280 and 365 nm light sources, accompanied by the luminescence change between blue and green. By taking advantages of this fascinating photo-responsive property, the material has been used to fabricate **2** + **3** heterostructured crystals using a photolithography technique, which can serve as an erasable photonic barcode. Moreover, photomechanical response was observed for **3** and **2** due to the internal strain at the interface of the reactant–product heterostructure, making it possible for the fabrication of photoactuators. This work provides a feasible strategy for the fabrication of MOF-based heterostructured crystals *via* the reversible [4 + 4] photocycloaddition reaction of anthracene and may shed light on the development of intelligent MOF-based heterostructures for photonic applications.

Data availability

The experimental and computational data have been provided in the ESI.†

Author contributions

X.-D. H. and B.-K. H. contributed equally to this work. X.-D. H. designed the study, conducted most of the experiments and wrote the draft of the manuscript. B.-K. H. and S.-H. L. performed the calculation and wrote the related discussion. G.-H. W. assisted in performing the single-crystal X-ray diffraction data collection. L.-M. Z. conceived the project and revised the manuscript.

Conflicts of interest

There are no conflicts to declare.

Acknowledgements

This work was supported by grants from the National Natural Science Foundation of China (21731003, 22273037) and the National Key R&D Program of China (2018YFA0306004).

Notes and references

1 (*a*) M. Pan, W.-M. Liao, S.-Y. Yin, S.-S. Sun and C.-Y. Su, *Chem. Rev.*, 2018, **118**, 889–918; (*b*) J. M. Cain, W. He, I. Maurin, M. W. Meisel and D. R. Talham, *J. Appl. Phys.*, 2021, **129**, 160903; (*c*) M. L. Foo, R. Matsuda and S. Kitagawa, *Chem. Mater.*, 2014, **26**, 310–322.

2 (*a*) R. Haldar and C. Wöll, *Nano Res.*, 2021, **14**, 355–368; (*b*) X.-T. Liu, K. Wang, Z. Chang, Y.-H. Zhang, J. Xu, Y.-S. Zhao and X.-H. Bu, *Angew. Chem., Int. Ed.*, 2019, **58**, 13890–13896; (*c*) Y. Yao, Z. Gao, Y. Lv, X. Lin, Y. Liu, Y. Du, F. Hu and Y. S. Zhao, *Angew. Chem., Int. Ed.*, 2019, **58**, 13803–13807; (*d*) G. Lee, S. Lee, S. Oh, D. Kim and M. Oh, *J. Am. Chem. Soc.*, 2020, **142**, 3042–3049; (*e*) C. R. R. Adolf, S. Ferlay, N. Kyritsakas and M. W. Hosseini, *J. Am. Chem. Soc.*, 2015, **137**, 15390–15393; (*f*) K. C. Jayachandrababu, D. S. Sholl and S. Nair, *J. Am. Chem. Soc.*, 2017, **139**, 5906–5915; (*g*) J. A. Boissonnault, A. G. Wong-Foy and A. Matzger, *J. Am. Chem. Soc.*, 2017, **139**, 14841–14844.

3 Y.-J. Ma, X. Fang, G. Xiao and D. Yan, *Angew. Chem., Int. Ed.*, 2022, **61**, e20211410.

4 (*a*) D. Venkatakrishnarao, M. A. Mohiddon, N. Chandrasekhar and R. Chandrasekar, *Adv. Opt. Mater.*, 2015, **3**, 1035–1040; (*b*) H. Xia, J. Cheng, L. Zhu, K. Xie, Q. Zhang, D. Zhang and G. Zou, *ACS Appl. Mater. Interfaces*, 2019, **11**, 15969–15976.

5 (*a*) A. M. Rice, C. R. Martin, V. A. Galitskiy, A. A. Berseneva, G. A. Leith and N. B. Shustova, *Chem. Rev.*, 2020, **120**, 8790–8813; (*b*) W. Danowski, T. v. Leeuwen, W. R. Browne and B. L. Feringa, *Nanoscale Adv.*, 2021, **3**, 24–40.

6 (*a*) X.-D. Huang, Y. Xu, K. Fan, S.-S. Bao, M. Kurmoo and L.-M. Zheng, *Angew. Chem., Int. Ed.*, 2018, **57**, 8577–8581; (*b*) X.-D. Huang, J.-G. Jia, M. Kurmoo, S.-S. Bao and L.-M. Zheng, *Dalton Trans.*, 2019, **48**, 13769–13779; (*c*) X.-D. Huang, G.-H. Wen, S.-S. Bao, J.-G. Jia and L.-M. Zheng, *Chem. Sci.*, 2021, **12**, 929–937.

7 (*a*) X.-D. Huang, X.-F. Ma, T. Shang, Y.-Q. Zhang and L.-M. Zheng, *Inorg. Chem.*, 2022, 61, DOI: **10.1021/acs.inorgchem.2c01210**; (*b*) X.-F. Ma, Y. Guo, X.-D. Huang, G.-H. Wen, S.-S. Bao, Y.-Q. Zhang and L.-M. Zheng, *Dalton Trans.*, 2022, **51**, 12026–12030.

8 (*a*) J.-C. Liu, X.-D. Huang, Q. Zou, S.-S. Bao, X.-Z. Wang, J.-Y. Ma and L.-M. Zheng, *J. Mater. Chem. C*, 2020, **8**, 7369–7377; (*b*) Q. Zou, T. Shang, X.-D. Huang, Q.-Q. Guo, J.-G. Jia, S.-S. Bao, Y.-Q. Zhang and L.-M. Zheng, *J. Mater. Chem. C*, 2021, **9**, 10749–10758; (*c*) Q. Zou, J.-C. Liu, X.-D. Huang, S.-S. Bao and L.-M. Zheng, *Chin. Chem. Lett.*, 2021, **32**, 1519–1522; (*d*) Q. Zou, S.-S. Bao, X.-D. Huang, G.-H. Wen, J.-G. Jia, L.-Q. Wu and L.-M. Zheng, *Chem.–Asian J.*, 2021, **16**, 1456–1465; (*e*) G. Collet, T. Lathion, C. Besnard, C. Piguet and S. Petoud, *J. Am. Chem. Soc.*, 2018, **140**, 10820–10828; (*f*) Q. Zou, G.-L. Wang, Y.-Q. Chen, X.-D. Huang, G.-H. Wen, M.-F. Qin, S.-S. Bao, Y.-Q. Zhang and L.-M. Zheng, *Chem.–Eur. J.*, 2023, e202203454.

9 X.-D. Huang, M. Kurmoo, S.-S. Bao, K. Fan, Y. Xu, Z.-B. Hu and L.-M. Zheng, *Chem. Commun.*, 2018, **54**, 3278–3281.

10 (*a*) X.-Y. Chen, H. Chen, L. Đorđevic, Q.-H. Guo, H. Wu, Y. Wang, L. Zhang, Y. Jiao, K. Cai, H. Chen, C. L. Stern, S. I. Stupp, R. Q. Snurr, D. Shen and J. F. Stoddart, *J. Am. Chem. Soc.*, 2021, **143**, 9129–9139; (*b*) M. Tu, H. Reinsch, S. Rodríguez-Hermida, R. Verbeke, T. Stassin, W. Egger,

M. Dickmann, B. Dieu, J. Hofkens, I. F. J. Vankelecom and N. Stock, *Angew. Chem., Int. Ed.*, 2019, **58**, 2423–2427.

11 (*a*) G. Kresse and J. Hafner, *Phys. Rev. B: Condens. Matter Mater. Phys.*, 1993, **47**, 558; (*b*) G. Kresse and J. Furthmüller, *Comput. Mater. Sci.*, 1996, **6**, 15–50; (*c*) G. Kresse and J. Furthmüller, *Phys. Rev. B: Condens. Matter Mater. Phys.*, 1996, **54**, 11169–11185.

12 G. Kresse and D. Joubert, *Phys. Rev. B: Condens. Matter Mater. Phys.*, 1999, **59**, 1758–1775.

13 (*a*) J. P. Perdew, K. Burke and M. Ernzerhof, *Phys. Rev. Lett.*, 1996, **77**, 3865–3868; (*b*) J. P. Perdew, K. Burke and M. Ernzerhof, *Phys. Rev. Lett.*, 1997, **78**, 1396.

14 (*a*) S. Grimme and J. Antony, *et. al.*, *J. Chem. Phys.*, 2010, **132**, 154104; (*b*) S. Grimme, S. Ehrlich and L. Goerigk, *J. Comput. Chem.*, 2011, **32**, 1456–1465.

15 M. Topsakal and R. M. Wentzcovitch, *Comput. Mater. Sci.*, 2014, **95**, 263–270.

16 (*a*) Y. Zhang, L. Zhang, R. Deng, J. Tian, Y. Zong, D. Jin and X. Liu, *J. Am. Chem. Soc.*, 2014, **136**, 4893–4896; (*b*) Z. Gao, B. Xu, T. Zhang, Z. Liu, W. Zhang, X. Sun, Y. Liu, X. Wang, Z. Wang, Y. Yan, F. Hu, X. Meng and Y.-S. Zhao, *Angew. Chem., Int. Ed.*, 2020, **59**, 19060–19064; (*c*) M. Pan, Y.-X. Zhu, K. Wu, L. Chen, Y.-J. Hou, S.-Y. Yin, H.-P. Wang, Y.-N. Fan and C.-Y. Su, *Angew. Chem., Int. Ed.*, 2017, **56**, 14582–14586; (*d*) G. Zhan and H.-C. Zeng, *Nat. Commun.*, 2018, **9**, 3778.

17 (*a*) P. Naumov, S. Chizhik, M. K. Panda, N. K. Nath and E. Boldyreva, *Chem. Rev.*, 2015, **115**, 12440–12490; (*b*) T. Kim, L. Zhu, R. O. Al-Kaysi and C. J. Bardeen, *ChemPhysChem*, 2014, **15**, 400–414; (*c*) B. Zhou and D. Yan, *Appl. Phys. Rev.*, 2021, **8**, 041310; (*d*) F. Tong, W. Xu, M. Al-Haidar, D. Kitagawa, R. O. Al-Kaysi and C. J. Bardeen, *Angew. Chem., Int. Ed.*, 2018, **57**, 7080–7084; (*e*) Q. Yu, M. Li, J. Gao, P. Xu, Q. Chen, D. Xing, J. Yan, M. J. Zaworotko, J. Xu, Y. Chen, P. Cheng and Z. Zhang, *Angew. Chem., Int. Ed.*, 2019, **58**, 18634–18640.

18 (*a*) T. Kim, L. L. Zhu, J. Mueller and C. J. Bardeen, *J. Am. Chem. Soc.*, 2014, **136**, 6617–6625; (*b*) A. Fujimoto, N. Fujinaga, R. Nishimura, E. Hatano, L. Kono, A. Nagai, A. Sekine, Y. Hattori, Y. Kojima, N. Yasuda, M. Morimoto, S. Yokojima, S. Nakamura, B. L. Feringa and K. Uchida, *Chem. Sci.*, 2020, **11**, 12307–12315.

19 (*a*) Y.-X. Shi, W.-H. Zhang, B. F. Abrahams, P. Braunstein and J.-P. Lang, *Angew. Chem., Int. Ed.*, 2019, **58**, 9453–9458; (*b*) B. B. Rath and J. J. Vittal, *J. Am. Chem. Soc.*, 2020, **142**, 20117–20123.

20 (*a*) J.-s. Geng, L. Mei, Y.-y. Liang, L.-y. Yuan, J.-p. Yu, K.-q. Hu, L.-h. Yuan, W. Feng, Z.-f. Cha and W.-q. Shi, *Nat. Commun.*, 2022, **13**, 2030; (*b*) A. K. Bartholomew, I. B. Stone, M. L. Steigerwald, T. H. Lambert and X. Roy, *J. Am. Chem. Soc.*, 2022, **144**, 16773–16777; (*c*) B. B. Rath and J. J. Vitta, *CrystEngComm*, 2021, **23**, 5738–5752; (*d*) S. Khan, Akhtaruzzaman, R. Medishetty, A. Ekka and M. H. Mir, *Chem.–Asian J.*, 2021, **16**, 2806–2816.